Plasma-Assisted Synthesis of Co₃O₄-Based Electrocatalysts on Ni Foam Substrates for the Oxygen Evolution Reaction

Chiara Maccato, Lorenzo Bigiani, Leonardo Girardi, Alberto Gasparotto,*
Oleg I. Lebedev, Evgeny Modin, Davide Barreca,* and Gian Andrea Rizzi

Electrocatalytic oxygen evolution reaction (OER) plays a key role in sustainable energy conversion and storage, but is severely hampered by the lack of efficient catalysts, whose development remains a critical and challenging issue. Herein, it is reported for the first time that pure and Fe_2O_3-containing Co_3O_4-based OER electrocatalysts are grown on highly porous Ni foams by plasma enhanced-chemical vapor deposition and/or radiofrequency sputtering. Thanks to the inherent advantages of cold plasma synthesis routes, Ni foam supports are efficiently infiltrated by Co_3O_4 nanostructures and eventually nanosized Fe_2O_3, allowing a fine-tuning of their mutual content, nano-organization, and oxygen defectivity. For Co_3O_4-Fe_2O_3 systems, these issues enable current densities up to ≈120 mA cm^{-2} at 1.79 V versus the reversible hydrogen electrode, an overpotential of ≈350 mV at 10 mA cm^{-2} and a Tafel slope as low as 60 mV dec^{-1}, favorably comparing with literature values for most cobalt-based OER catalysts reported so far. Such features, accompanied by a good time stability, represent an important goal for eventual practical applications and candidate the proposed fabrication route as a valuable tool for the design of efficient electrocatalysts with precisely engineered properties and based on naturally abundant transition elements.

C. Maccato, L. Bigiani, L. Girardi, A. Gasparotto, G. A. Rizzi
Department of Chemical Sciences
Padova University and INSTM
Padova 35131, Italy
E-mail: alberto.gasparotto@unipd.it

O. I. Lebedev
Laboratoire CRISMAT
UMR 6508 CNRS/ENSICAEN/UCBN
Caen Cedex 4 14050, France

E. Modin
CIC nanoGUNE BRTA
Donostia, San Sebastian 20018, Spain

D. Barreca
CNR-ICMATE and INSTM
Department of Chemical Sciences
Padova University
Padova 35131, Italy
E-mail: davide.barreca@unipd.it

The ORCID identification number(s) for the author(s) of this article can be found under https://doi.org/10.1002/admi.202100763.

1. Introduction

Oxygen evolution reaction (OER) is the most imperative process for several energy conversion and storage devices, encompassing fuel cells, water splitting systems, and metal-air batteries, but its efficiency is severely limited by the multiple-electron transfer elementary steps, resulting in a significant energy barrier.[1–9] Although precious metal oxides, such as those of Ru and Ir, have proven to be catalytically efficient in triggering OER processes, their high cost, and rarity, along with the limited long-term stability, make them unfeasible on an industrial scale.[1,3,4,6,9,10] As a consequence, extensive research efforts have been focused on the development of cost-effective and earth-abundant OER anodic catalysts featuring an appreciable activity and a sufficient service life for practical end-uses.[5,11–15] In this context, spinel-type Co_3O_4 has emerged as an attractive candidate thanks to its mixed Co(II)/Co(III) valency, tunable defect chemistry, low price, and good operational stability.[7,12,16,17] Nevertheless, since bulk Co_3O_4 presents a low surface area and—similarly to many transition metal oxides—suffers from a modest electronic conductivity, the full exploitation of its electrochemical performances inevitably requires a tailored design and engineering of the anode structure.[5,16,18–23] To this aim, important degrees of freedom are offered by a proper choice of the substrate, the modulation of the catalyst properties, and, eventually, the introduction of suitable co-catalysts, whose synergistic interactions with Co_3O_4 may afford a favorable improvement of the resulting electrochemical behavior. As concerns the substrate, the use of porous and highly conductive scaffolds enables an efficient catalyst dispersion and adhesion on the substrate, providing thus favorable pathways for both mass and charge transport.[13,20,24,25] Among the various options,[18,26] metallic nickel foams have received increasing attention since they combine a remarkable electrical conductivity with a high active area arising from a continuous 3D open-pore structure.[13,24,27–29] In addition, the nanoscale control of Co_3O_4 characteristics, including exposed crystallographic facets and oxygen vacancy content, are effective means to enhance electrical conductivity and tailor material reactivity,[5,17,30–34] improving the ultimate catalytic performances.[1,2,5,6,11,12,16,21,22,26,35] The latter can be further boosted by functionalization of Co_3O_4 with a suitable

**ADVANCED
SCIENCE NEWS**

www.advancedsciencenews.com

**ADVANCED
MATERIALS
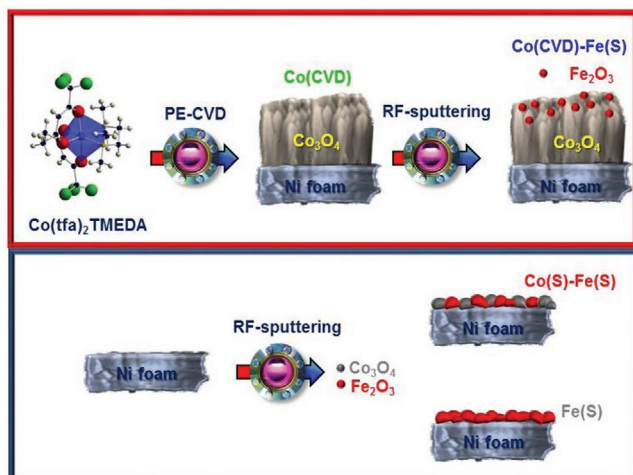INTERFACES**

www.advmatinterfaces.de

Figure 1. Sketch of the plasma-assisted route adopted for the preparation of the target materials. The various specimens are labeled as follows: Co_3O_4 nanostructures grown by PE-CVD → Co(CVD); PE-CVD grown Co_3O_4 nanostructures functionalized with Fe_2O_3 NPs by RF-sputtering → sample Co(CVD)-Fe(S); intermixed Co_3O_4-Fe_2O_3 NPs fabricated by RF-sputtering → Co(S)-Fe(S); bare Fe_2O_3 fabricated by RF-sputtering → Fe(S).

co-catalyst, often a second nanostructured metal oxide. Successful examples include Co_3O_4 coupling with Fe_2O_3, NiO, CuO, or ZnO nanoparticles (NPs),[26,36–39] whose introduction can result in an increased amount of active sites, and promote a synergistic catalytic/electronic interplay between the system components.[26,36–38,40–42] To this aim, a key role is played by the successful implementation of flexible preparative strategies allowing a direct control over material morphology, structure, and composition. In this regard, plasma-assisted routes such as plasma enhanced-chemical vapor deposition (PE-CVD) and radiofrequency (RF) sputtering, benefitting from the unique properties of cold-plasmas,[6,43–45] represent versatile techniques for the production of functional nanomaterials with tailored properties. The utility and flexibility of cold plasmas for the above routes are due to their high chemical reactivity even in the absence of external thermal supplies, enabling material processing at temperatures lower than the ones used in conventional routes.[46] The bombardment of the growing surface by accelerated heavy species might result in the development of specific growth directions and/or in the obtainment of metastable crystal phases, peculiar morphologies, and highly defective structures.[6,16,44,47,48] In the case of porous substrates, such as Ni foams, ion bombardment and the associated local energy transfer are responsible for an inherent infiltration power, enabling an effective catalyst (and eventually co-catalyst) dispersion into the substrate pores system.[20,43,45,47,49] These effects, combined with the excitation, ionization, and dissociation of gas molecules promoted by "hot" electrons, enable the activation of a unique gas-phase and surface chemistry, diversifying material features from those obtained by standard vapor-phase routes.[44] In general, deposition, ablation, and surface modification processes are concurrent and the predominance of one over the others can be obtained by a proper choice of the experimental conditions. In particular, the ubiquitous competition between deposition and ablation phenomena limits particle growth at the

nanoscale and favors the formation of a high density of interfaces,[20,44,45] a favorable issue for the target applications. Finally, the above techniques enable the growth of the catalyst directly over the substrate, resulting in enhanced stability and avoiding thus disadvantages typical of powdered materials.[2,13,20,25,27,39,43]

In the present work, pure and Fe_2O_3-containing Co_3O_4-based electrocatalysts are grown on porous Ni foams according to the fabrication route sketched in **Figure 1**. Specifically, Co_3O_4 nanostructures are synthesized by PE-CVD and eventually decorated via RF-sputtering with Fe_2O_3 NPs as co-catalysts.[18,20,31,32,50] For comparison, RF-sputtering is also used to deposit intermixed Co_3O_4-Fe_2O_3 NPs or bare Fe_2O_3 directly on Ni foams.

After a detailed structural, compositional, and morphological investigation of the obtained systems, the same are preliminarily tested as OER electrocatalysts, devoting particular attention to the interplay between material physicochemical characteristics and functional performances.

2. Results and Discussion

2.1. Material Characterization

Preliminary structural characterization of the target materials was performed through X-ray diffraction (XRD). For samples Co(CVD) and Co(CVD)-Fe(S), the recorded patterns (Figure S1, Supporting Information) showed two signals at $2\theta = 31.1°$ and $36.6°$ ascribed respectively to the (220) and (311) crystallographic planes of cubic spinel-type Co_3O_4.[17,35,51,52] For specimen Co(CVD)-Fe(S), the lack of appreciable Co_3O_4 peak shifts in comparison to sample Co(CVD) allowed to exclude the occurrence of cobalt oxide doping by iron,[33,47] and was in line with the formation of a separate Fe-containing phase upon sputtering, as indeed confirmed below by transmission electron microscopy (TEM). In addition, the slight decrease of the overall diffracted intensity concerning specimen Co(CVD) was ascribed to plasma-surface interactions and ion bombardment of Co oxide upon Fe_2O_3 deposition.[53] This phenomenon was responsible for a concomitant increase of O defects content (see below and Figure S2, Supporting Information). The lack of reflections for samples Co(S)-Fe(S) and Fe(S) suggested that the mild RF-sputtering conditions adopted herein yielded the deposition of relatively low cobalt/iron oxide amounts,[20,54] as indeed confirmed by complementary analytical results (see below).

Information on material chemical composition was obtained by X-ray photoelectron spectroscopy (XPS). Wide-scan spectra (**Figure 2**a) revealed only a minor carbon contribution (10 at%) attributed to atmospheric contamination.[47,55,56] For samples Co(CVD) and Co(CVD)-Fe(S), the expected cobalt and oxygen signals were detected and accompanied by iron signals in the latter case. In line with the above XRD data, these results suggested a high dispersion of iron-containing particles into the pristine Co_3O_4,[20,54] without a complete coverage of the latter. The surface co-presence of both cobalt and iron was detected even for sample Co(S)-Fe(S), although in a different ratio (see below). For this specimen as well as for Fe(S), even nickel signals from the underlying substrate were observed, revealing that the adopted RF-sputtering conditions led to the deposition of low material amounts.[20,54]
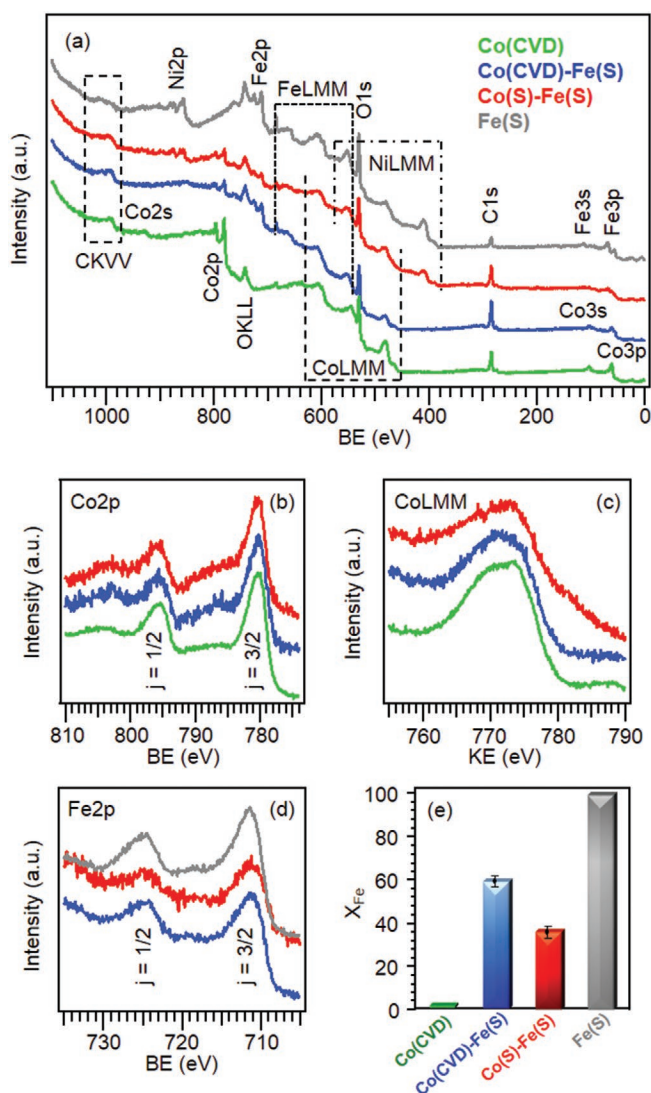
2100763 (2 of 10)

Figure 2. a) XPS survey spectra for the target specimens. b) Co2p, c) CoLMM (in kinetic energy, KE), and d) Fe2p photoelectron and Auger signals. Color codes as in panel (a). e) Iron surface molar fraction (X_{Fe}) for the target samples.

Valuable insights into the chemical state of the fabricated electrode materials were gained by the detailed analysis of the most representative Co, Fe, and O XPS photopeaks (Figures 2b-d and Figure S2, Supporting Information). Regardless of the synthesis conditions, the binding energy (BE) and spin-orbit-separation (SOS) of the Co2p peak [Figure 2b; BE(Co2p$_{3/2}$) = 780.2 eV; SOS = 15.2 eV], along with the low intensity of shake-up satellites, confirmed the formation of Co_3O_4 as the predominant cobalt oxide.[17,21,35,47,53,56,57] This conclusion was further supported by calculation of the cobalt Auger parameter (see also Figure 2c; α = 1552.6 eV).[47,56] As far as the Fe2p peak is concerned [Figure 2d; BE(Fe2p$_{3/2}$) = 711.2 eV; SOS = 13.4 eV], its spectral features were in good agreement with previous literature data for Fe_2O_3.[46,47,53]

Additional information was provided by the analysis of the O1s signals (Figure S2, Supporting Information, that resulted from a first component due to lattice oxygen

(I; mean BE = 529.9 eV)[8] and an additional band (II; average BE = 531.6 eV) attributed to hydroxyl groups chemisorbed on O defects.[6,17,46,47,52] The latter band amounted to 30%, 38%, 54%, and 47% of the total oxygen content in Co(CVD), Co(CVD)-Fe(S), Co(S)-Fe(S), and Fe(S) respectively. The increased content of oxygen vacancies is indeed beneficial in enhancing material performances in OER applications.[6,17,21,57,58] The higher surface defectivity of the last three specimens, arising from an effective plasma bombardment during the sputtering step (see above), might also be responsible for the appearance of the weak shake-up features on the high BE side of Co2p$_{3/2}$ and Co2p$_{1/2}$ bands for samples Co(CVD)-Fe(S) and Co(S)-Fe(S) (see Figure 2b).[21,35,48] This phenomenon suggests a concomitant slight surface reduction of Co_3O_4, in agreement with previous studies.[17,21,48,52,57,58]

Table S1 (Supporting Information) reports the Co, Fe, Ni, and O XPS atomic percentages for the various specimens, whereas the corresponding iron surface molar fraction, X_{Fe} (see Experimental Section), is displayed in Figure 2e. The latter parameter provides a fingerprint on the extent of Co_3O_4 surface functionalization by iron-based NPs. As can be observed, X_{Fe} could be tailored in the range 0–100% according to the adopted preparative conditions. More specifically, for samples Co(CVD)-Fe(S) and Co(S)-Fe(S), the obtained X_{Fe} values (60% and 37%, respectively) indicated the surface co-presence of cobalt and iron oxides in comparable amounts. As discussed in the following, this issue seems to play a beneficial role on the resulting OER performances.[41,58,59]

Subsequently, efforts were dedicated to the investigation of material morphology by field emission-scanning electron microscopy (FE-SEM) (**Figure 3**). As can be observed, pure Co_3O_4 [sample Co(CVD)] was characterized by an ordered array of elongated Co_3O_4 nanostructures (lateral size = 60 nm), evenly covering the underlying Ni foam substrate (Figure 3a). Upon functionalization with iron oxide [specimen Co(CVD)-Fe(S); Figure 3b], no significant alteration of the system morphology took place, in line with the mild sputtering conditions and the deposition of a low Fe_2O_3 amount.[20,54] Differently, for specimens Co(S)-Fe(S) and Fe(S) (see Figures 3c,d), the Ni foam support appeared homogeneously decorated by small, dispersed NPs with an average diameter ≤20 nm. Taking into account even the low amount of sputtered material (see also TEM results below), such morphology is in line with the detection of the Ni2p XPS signal (Table S1, Supporting Information).

A deeper insight into the system nanostructure was gained by cross-sectional TEM and energy dispersive X-ray spectroscopy (EDXS) measurements. For sample Co(CVD)-Fe(S), in line with FE-SEM observations, the obtained results confirmed the uniform Ni foam coverage by an array of anisotropic Co_3O_4 quasi-1D structures (mean length and width ≈700 and 50 nm, respectively; **Figure 4**a), growing almost perpendicularly to the substrate surface. As revealed by EDXS elemental mapping, Fe_2O_3 was evenly covering cobalt oxide structures and was mainly confined in the outermost material region. In line with XRD results (see above), high resolution (HR) TEM and electron diffraction (ED) investigation (Figure 4b) confirmed the presence of cubic spinel-type Co_3O_4 (space group: *Fd-3m(227)*, a = 8.07 Å, ICSD 36 256), while HRTEM imaging in combination with Fourier transform (FT) (Figure 4b inset) revealed its decoration by γ-Fe_2O_3 (space group: *Fd-3m*(227),
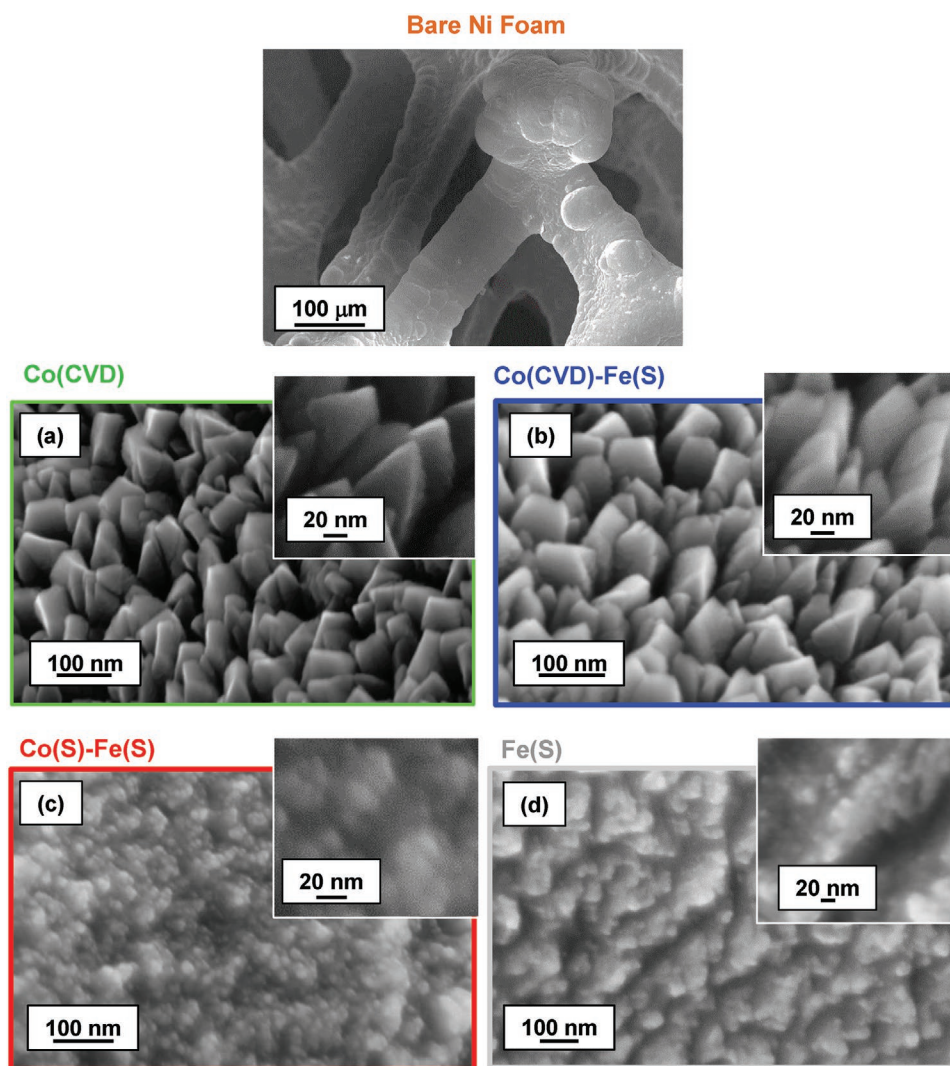
Bare Ni Foam

Figure 3. Representative FE-SEM micrographs for Co(CVD) (a), Co(CVD)-Fe(S) (b), Co(S)-Fe(S) (c), and Fe(S) (d) electrodes. In each case, higher magnification images are shown as insets. The morphology of the bare Ni foam is also shown in the top panel.

a = 8.37 Å, ICSD 247 034) NPs (average dimensions = 4 nm). In line with previous studies, the occurrence of γ-Fe$_2$O$_3$ instead of the thermodynamically stable α-Fe$_2$O$_3$ phase was traced back to the unique nonequilibrium conditions characterizing the present plasma-assisted synthetic strategy.[20,54] Nonetheless, maghemite formation can also be favored by its structural similarity with spinel-type Co$_3$O$_4$, both belonging to the cubic *Fd-3m* system and possessing similar unit cell parameters. Overall, the 1D morphology of the present Co$_3$O$_4$ nanostructures and the functionalization of their tips by low-sized γ-Fe$_2$O$_3$ aggregates anticipates a high number of active surface sites, a promising issue in view of OER applications.[37,40]

Concerning sample Co(S)-Fe(S), a different material nano-organization was observed (**Figure 5**). The deposit had an overall thickness ranging between 10 and 20 nm—much lower than the previous specimen—and was formed by intermixed Co$_3$O$_4$ and Fe$_2$O$_3$ pseudo-spherical NPs with a typical size of ≈5–8 nm. Altogether, such aggregates formed a thin and relatively porous layer, a feature in line with the detection of Ni2p

signal revealed by surface XPS analyses. The strong intermixing between Co$_3$O$_4$ and Fe$_2$O$_3$ phases and the high density of the resulting heterointerfaces, whose occurrence was promoted by the adopted plasma-assisted preparative strategy, might produce synergistic catalytic and electronic effects favorable for OER applications. Additional benefits in this regard arise from the reduced particle size, which, in turn, favors charge transport phenomena,[26,37,38,40,41] suppressing detrimental recombination losses. For sample Fe(S) (Figure S3, Supporting Information), the Fe$_2$O$_3$ deposit appeared morphologically similar to the previous one, and, accordingly, the formation of γ-Fe$_2$O$_3$ took place even in this case.

2.2. Electrochemical Tests

A preliminary assessment of OER performances of the developed materials was assessed by electrochemical measurements in 1 M KOH solutions. Linear sweep voltammetry (LSV) (**Figure 6**a)
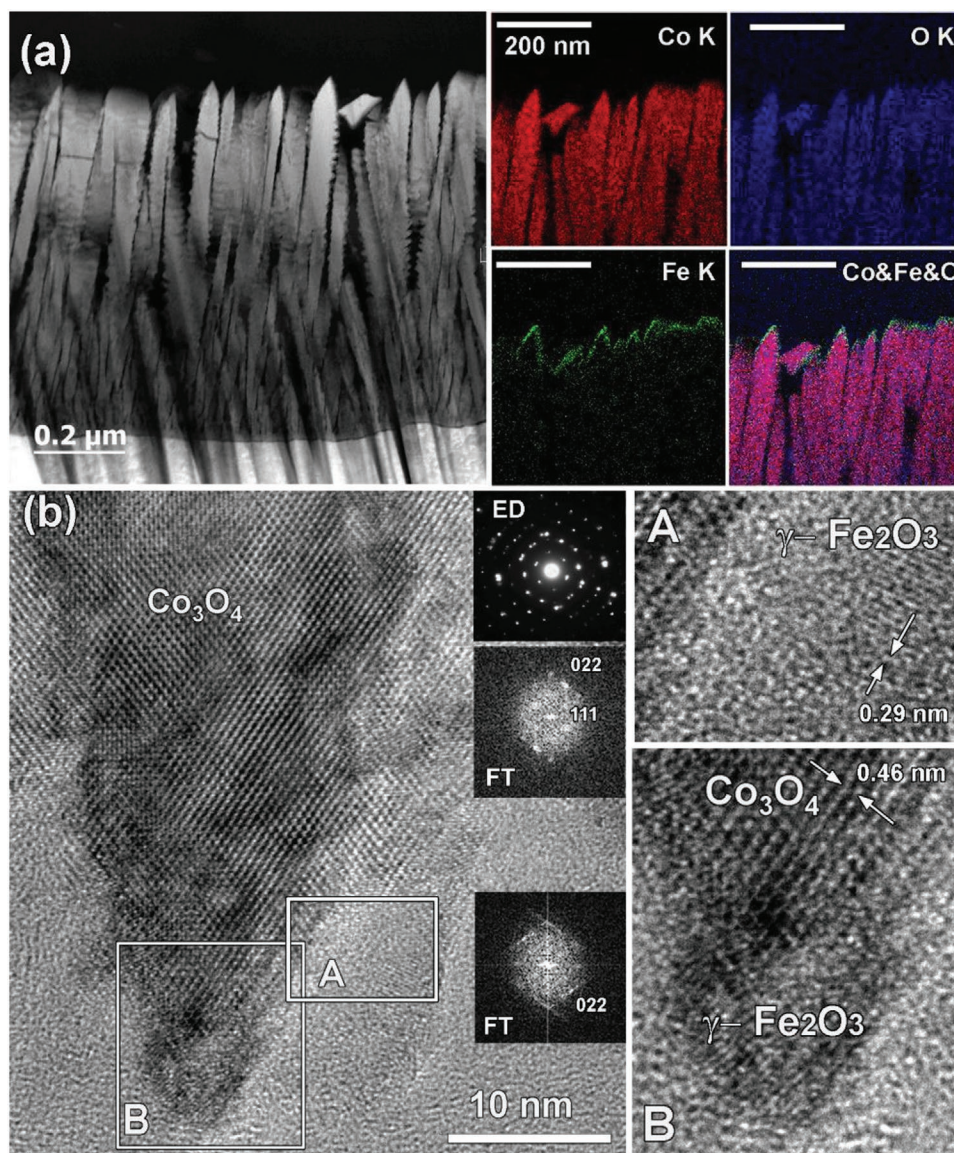
2100763 (4 of 10)

Figure 4. a) Low magnification HAADF-STEM cross-sectional image and corresponding EDXS elemental maps for sample Co(CVD)-Fe(S). b) HRTEM micrograph and ED pattern (inset in the upper right corner) for the same specimen, confirming Co_3O_4 decoration by γ-Fe_2O_3 nanoparticles. The magnified images of A and B regions (marked by white boxes) and corresponding FT patterns refer to γ-Fe_2O_3 nanostructure viewed along [112] and [110] zone axes.

and cyclic voltammetry (CV) curves (Figure S4, Supporting Information) were all characterized by an anodic feature corresponding to the M-O → M-O(OH) conversion process, a phenomenon typically observed for metal oxide structures in alkaline solutions under the application of relatively high potentials.[52,59,60] In addition, LSV curves revealed that, for all samples, the overpotential required to achieve a current density of 10 mA cm^{-2} was systematically lower than that of the bare Ni substrate, and increased in the order Co(S)-Fe(S) < Fe(S) < Co(CVD)-Fe(S) < Co(CVD) < Ni foam (**Table 1**) suggesting a higher activity for specimens obtained by direct RF-sputtering on Ni foam and, in particular, for the Co(S)-Fe(S) system. Indeed, the Co(S)-Fe(S) sample exhibited an overpotential 50 mV lower than the bare Ni foam, and 30 mV lower than Co(CVD)-Fe(S), which had a similar composition but different

morphological and structural features. On the other hand, the Co(CVD)-Fe(S) sample outperformed all the others as regards current density values at high potentials. In particular, at 1.79 V versus reversible hydrogen electrode (RHE) (Table 1), Co(CVD)-Fe(S) showed a current density 57% higher than Ni foam and 30% higher than Co(CVD), confirming the beneficial role of γ-Fe_2O_3 functionalization on the resulting electrocatalytic performances.

In line with previous investigations,[61,62] Tafel plots were hence calculated from LSV curves to obtain further information about reaction kinetics (Figure 6b). The obtained slopes (Table 1) decreased in the order Ni foam > Co(CVD) > Fe(S) > Co(S)-Fe(S) > Co(CVD)-Fe(S), suggesting thus a faster reaction kinetics for the latter specimen.[20,32] In general, a Tafel slope decrease can be ascribed to changes in the reaction mechanism
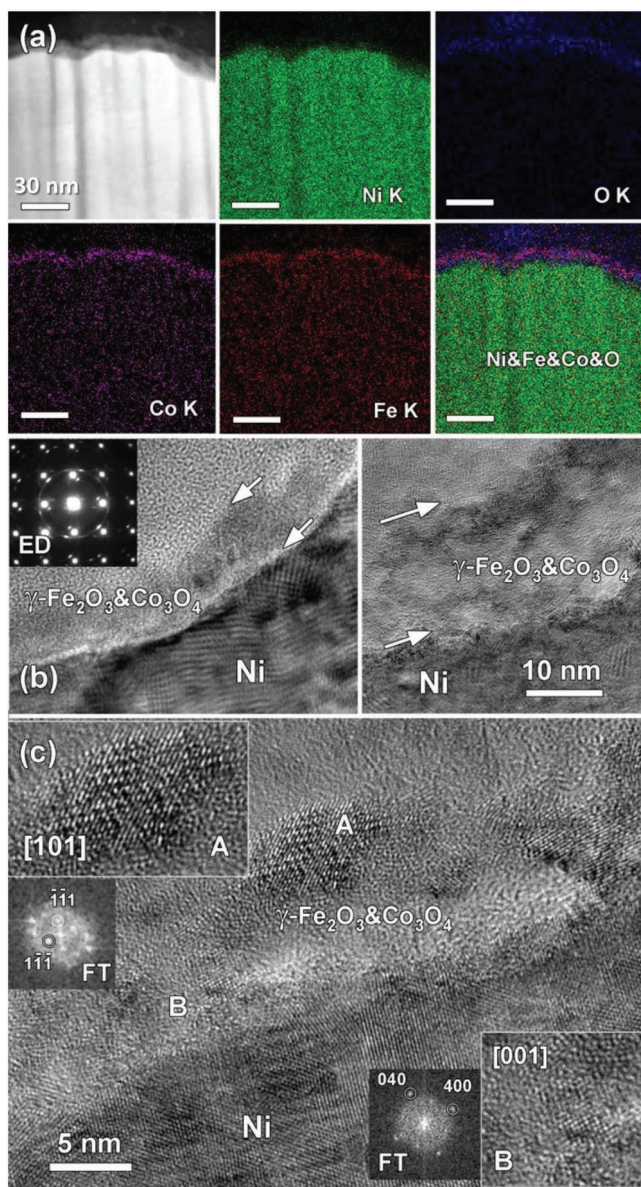
**ADVANCED
SCIENCE NEWS**
www.advancedsciencenews.com

**ADVANCED
MATERIALS
INTERFACES**
www.advmatinterfaces.de

Figure 5. a) Low magnification HAADF-STEM cross-sectional image and corresponding EDXS elemental maps for Co(S)-Fe(S). b) HRTEM images and corresponding ED pattern for the same specimen, showing the Ni foam coverage by a composite Co_3O_4-Fe_2O_3 layer (marked by the white arrows). c) Representative HRTEM micrograph and pertaining higher resolution images, with corresponding FT patterns of γ-Fe_2O_3 nanoparticles viewed along the [101] zone axis (A, upper left corner) and [001] zone axis (B, bottom right corner). FT patterns were indexed basing on the cubic γ-Fe_2O_3 structure.

(the Tafel slope decreases once the rate-determining step is closer to the end step of a series of reactions) and/or to a different degree of surface coverage by reaction intermediates (the higher the coverage, the lower the corresponding Tafel slope) even for the same rate-determining step.[4,63,64] The former effect could account for the improved performances of composite materials with respect to single component ones. In fact, synergistic Co_3O_4/Fe_2O_3 interactions could favorably affect the reaction mechanism inducing a shift toward the last

reaction of the four-step OER mechanism, reducing thus both overpotential and Tafel slope values.[4,59,64] On the other hand, the higher current density of Co(CVD)-Fe(S) with respect to Co(S)-Fe(S) at high potentials (>1.75 V versus RHE) can be explained basing on the following issues. As evidenced by TEM analyses, in the case of Co(CVD)-Fe(S), the Ni substrate is covered by a deposit endowed with an open structure whose surface area is deemed to be higher than that of Co(S)-Fe(S). The latter sample, conversely, showed a distribution of fine-grained Co_3O_4-Fe_2O_3 intermixed NPs forming a discontinuous thin layer on the Ni foam substrate. These characteristics suggested a faster charge carrier transfer from the active sites to the external circuit in the case of Co(S)-Fe(S), accounting thus for its lower overpotential.[30] As a matter of fact, the higher surface area of Co(CVD)-Fe(S) (see C_{DL} values in Table 1) with respect to Co(S)-Fe(S) favors the presence of a higher number of active sites and, in turn, a higher degree of surface coverage by reaction intermediates. These issues are responsible for the lower Tafel slope of sample Co(CVD)-Fe(S), and may account for its enhanced current density at high potentials.[30,59]

The above explanation is further corroborated by the evaluation of current density differences (Δj) versus the applied potential between thick and large-area deposits [i.e., Co(CVD) and Co(CVD)-Fe(S)], and thin discontinuous ones [i.e., Co(S)-Fe(S) and Fe(S)] (**Figure 7**a). In all cases, two regions can be identified in the plot. At low applied potentials (grey regions in Figure 7a), Δj values decreased, revealing a faster increase of current density for Co(S)-Fe(S) and Fe(S) samples, whereas at high potentials [>1.65 V for Co(CVD)-Fe(S), >1.73 V for Co(CVD); red regions in Figure 7a] Δj values increased indicating a faster current density rise for Co(CVD)-Fe(S) and Co(CVD). In other words, at low applied potentials, thin deposits [Co(S)-Fe(S) and Fe(S)] benefit from shorter charge carrier pathways (Figure 7b, top). In addition, in the case of specimen Co(S)-Fe(S), its higher oxygen defectivity and the synergistic interaction between Co_3O_4 and Fe_2O_3 (see above) further boost the ultimate OER performances. Conversely, the higher resistivity of the thicker Co_3O_4 layer, deposited by PE-CVD, requires larger potentials to promote holes migration toward the outermost surface (electrons migration toward the external circuit) where a large number of active sites allows the efficient adsorption/activation of reactants and intermediates, sustaining thus high current densities.

As a consequence, thick porous deposits, i.e., Co(CVD) and especially Co(CVD)-Fe(S), show the best electrocatalytic activity (Figure 7b, bottom). This conclusion is further confirmed by electrochemical impedance spectroscopy (EIS) data (Figure S5, Supporting Information), clearly showing that the more resistive samples are the ones containing the Co_3O_4 deposit grown by PE-CVD, whereas lower resistance values were found in specimens fabricated by RF-sputtering. Regarding these results, it is also worthwhile highlighting that functionalization with Fe_2O_3 has a significant beneficial effect on the electrocatalytic properties of the Co_3O_4 deposit synthesized by PE-CVD. In fact, the charge transfer resistance of Co(CVD)-Fe(S) is strongly reduced if compared with specimen Co(CVD). Remarkably, the overpotential and Tafel slope values of the developed electrocatalysts compare favorably with other Co-based systems reported in the literature so far (see Table S2, Supporting Information).
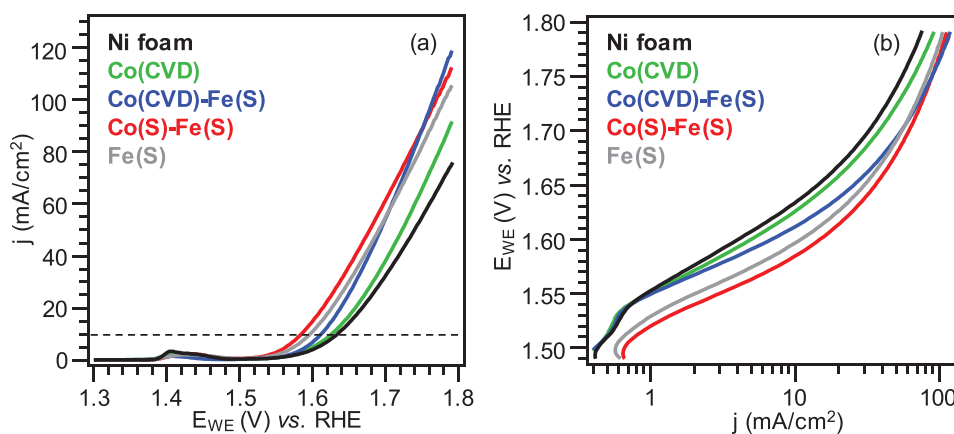
Figure 6. Electrochemical performances of Co(CVD), Co(CVD)-Fe(S), Co(S)-Fe(S), Fe(S), and bare Ni foam in 1.0 M KOH media: a) LSV curves. The horizontal dashed line marks the current density of 10 mA cm^{-2}; b) corresponding Tafel plots.

The time stability of the developed materials was investigated by means of chronoamperometry (CA) for 15 h at a fixed potential of 1.65 V versus RHE. As can be observed from an inspection to **Figure 8**a, Co(S)-Fe(S) and Fe(S) exhibited a trend similar to that of the bare Ni foam, characterized by a slight current density increase during the first 1–2 h, followed by a j value decrease of 17%, 20%, 31% for Fe(S), Co(S)-Fe(S), and Ni foam, respectively. In a different way, in the case of specimens Co(CVD) and Co(CVD)-Fe(S), the measured current density increased during the first 4 h of testing, and subsequently underwent only a very modest decrease (3%, for Co(CVD); 9%, for Co(CVD)-Fe(S)), an important prerequisite in view of practical end uses. In order to further verify the occurrence of possible material deterioration, LSV curves were recorded again after CA experiments (Figure 8b). For each of the analyzed specimens, the j versus E_{RHE} trend was almost identical to the pertaining one collected before chronoamperometric measurements (compare Figure 8b with Figure 6a), enabling thus to rule out any appreciable corrosion phenomenon. Taken together, the present results highlight Co(CVD)-Fe(S) as the best performing system among those investigated in the present work.

3. Conclusion

In summary, pure and Fe$_2$O$_3$-containing Co$_3$O$_4$-based OER electrocatalyst materials with tailored compositional and morphological properties were fabricated by an original plasma-assisted strategy. Specifically, Co$_3$O$_4$ quasi-1D nanostructures were deposited on porous Ni foams by PE-CVD, and eventually decorated by a tiny amount of Fe$_2$O$_3$ NPs by RF-sputtering. The system structure and properties were analyzed in detail, and critically compared with those of thin and porous deposits composed by finely grained pure Fe$_2$O$_3$ or intermixed Co$_3$O$_4$-Fe$_2$O$_3$ NPs fabricated by sputtering.

The results obtained by a multi-technique characterization approach highlight that Co$_3$O$_4$ coupling with Fe$_2$O$_3$ successfully boosts OER functional behavior in comparison to single-phase materials, both in terms of activity and time stability. Preliminary electrocatalytic functional tests revealed that the best performances corresponded to current densities up to ≈120 mA cm^{-2} at 1.79 V versus RHE, an overpotential as low as ≈350 mV at 10 mA cm^{-2}, accompanied by a Tafel slope of only 60 mV dec^{-1}. The present findings were rationalized basing on concurring effects related to the catalyst morphology and nanoscale organization, as well as to its composition in terms of Co$_3$O$_4$/Fe$_2$O$_3$ ratio and oxygen defectivity. Overall, the obtained results revealed that a careful tailoring of such material characteristics empowers the functional behavior of Co$_3$O$_4$-based OER electrocatalysts, rendering them attractive alternatives to state-of-the-art anode materials based on rare and expensive metals such as Ru and Ir. Additional perspectives for research developments will concern CA stability tests on the fabricated materials for a duration ≥100 h, in view of eventual practical applications. Ultimately, the proposed synthetic approach, which can

Table 1. Relevant electrochemical parameters for the target materials: overpotentials required to reach a current density of 10 mA cm^{-2}, current densities at 1.79 V versus RHE, Tafel slopes related to the OER in 1.0 M KOH solution, and double layer capacitance (C_{DL}, normalized by the geometrical area) derived from CVs in the non-Faradaic region.

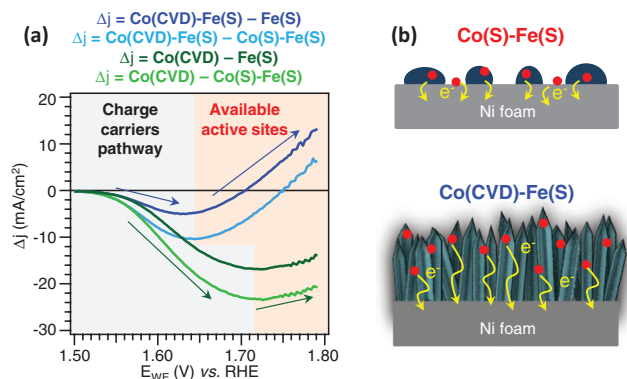| Material	Overpotential [mV]	j [mA cm^{-2}] @ 1.79 V vs. RHE	Tafel slope [mV dec^{-1}]	C_{DL} [mF cm^{-2}]
Ni foam	404	75	80	0.42
Co(CVD)	396	91	71	0.76
Co(CVD)-Fe(S)	382	118	60	0.63
Co(S)-Fe(S)	355	112	62	0.33
Fe(S)	366	105	66	0.41

Figure 7. a) Current density differences (Δj) as a function of the applied potential. b) Schematic representation of active sites (red spots) and charge carriers pathway (yellow arrows) in samples Co(S)-Fe(S) and Co(CVD)-Fe(S).

be operated under relatively mild processing conditions and without any surfactant or binder, offers amenable opportunities and guidelines for the design of high-performance electrocatalysts taking advantage on strong interactions between the single components at the nanometer scale.

4. Experimental Section

Material Preparation: The target materials were grown by PE-CVD and/or RF-sputtering on commercial Ni foams (Ni-4753, RECEMAT BV; thickness = 1.5 mm; lateral size = 1 × 1.5 cm²), following the procedure sketched in Figure 1. The substrates were preliminarily cleaned by sonication in dichloroethane (10 min), 3.5 M HCl (10 min), and ethanol (10 min)[19,25,27,28,65] and subsequently mounted on the ground electrode of a custom-built RF-powered (13.56 MHz) plasmochemical reactor.[46,47]

PE-CVD grown Co$_3$O$_4$-based materials [samples Co(CVD) and Co(CVD)-Fe(S)] were prepared starting from Co(tfa)$_2$TMEDA (tfa = 1,1,1-trifluoro-2,4-pentanedionate; TMEDA = *N,N,N',N'*-tetramethylethylenediamine) as the cobalt molecular source.[66] The compound was vaporized at 70 °C in an external glass reservoir and its vapors were transported into the PE-CVD reactor by an Ar flow [rate = 60 standard cubic centimeters

per minute (sccm)] through gas lines maintained at 130 °C by means of external heating tapes. Additional Ar and O$_2$ flows (rates = 15 and 5 sccm, respectively) were introduced into the reaction chamber through independent inlets. Basing on preliminary optimization experiments, depositions were performed for 180 min at a substrate temperature of 300 °C and a total pressure of 1.0 mbar, using an RF-power of 20 W. For the preparation of sample Co(CVD)-Fe(S), Fe$_2$O$_3$ NPs were dispersed over previously obtained PE-CVD Co$_3$O$_4$ by RF-sputtering in Ar plasmas (see Figure 1) from a Fe target (Alfa Aesar, 99.995%, 50 × 50 mm², thickness = 0.25 mm). Depositions were performed using the following settings: RF-power = 20 W; total pressure = 0.3 mbar; growth temperature = 60 °C; Ar flow rate = 10 sccm; process duration = 180 min.[20] The same process parameters were used for the fabrication of sample Co(S)-Fe(S) by RF-sputtering, yet starting from a Fe$_2$O$_3$-Co$_3$O$_4$ mixed target (Neyco, purity = 99.9%, 50 × 50 mm², thickness = 2 mm). Finally, a bare Fe$_2$O$_3$ sample [specimen Fe(S)] was also prepared as a reference by RF-sputtering from the above indicated iron target, using the same operating conditions adopted for the preparation of sample Co(CVD)-Fe(S).

Chemico-Physical Characterization: XRD measurements were performed in glancing incidence mode (θ_i = 1.0°) by a Bruker AXS D8 Advance Plus diffractometer equipped with a Göbel mirror and a CuKα X-ray source (λ = 1.54051 Å) powered at 40 kV, 40 mA.

XPS analyses were carried out on a Perkin–Elmer Φ 5600ci system, using a non-monochromatized MgKα excitation source ($h\nu$ = 1253.6 eV). Charging correction on BE values was carried out referencing the C1s peak at 284.8 eV.[55] Atomic percentages (at%) were obtained by peak integration using Φ V5.4A sensitivity factors. Data processing involved Shirley-type background subtraction, and, when necessary, spectral deconvolution through the XPSPEAK 4.1 software. The cobalt Auger parameter was calculated according to the following equation: α = BE(Co2p$_{3/2}$) + KE(CoLMM).[55] The iron surface molar fraction was defined as: X_{Fe} = [(Fe at%) / (Co at% + Fe at%)] × 100.[47]

FE-SEM images were collected on a Zeiss SUPRA 40VP microscope, operating at primary beam acceleration voltages of 10 kV and collecting electrons by means of an in-lens detector. The average particle size was estimated by processing high-resolution micrographs with the ImageJ software.[67]

Thin cross-sectional samples for TEM analyses were prepared using Helios 450s FIB/SEM (Thermo Fisher, USA) via a standard protocol by means of focused ion beam (FIB) technique. Pre-thinned lamellas were lifted-out from the material, attached to TEM grid and subsequently thinned down to electron transparency. Final cleaning was performed with FIB operating at 5 kV and 25 pA. Whenever necessary, a Pt protective layer was deposited during sample preparation to prevent the structures from collapsing. TEM analyses, including HRTEM, high
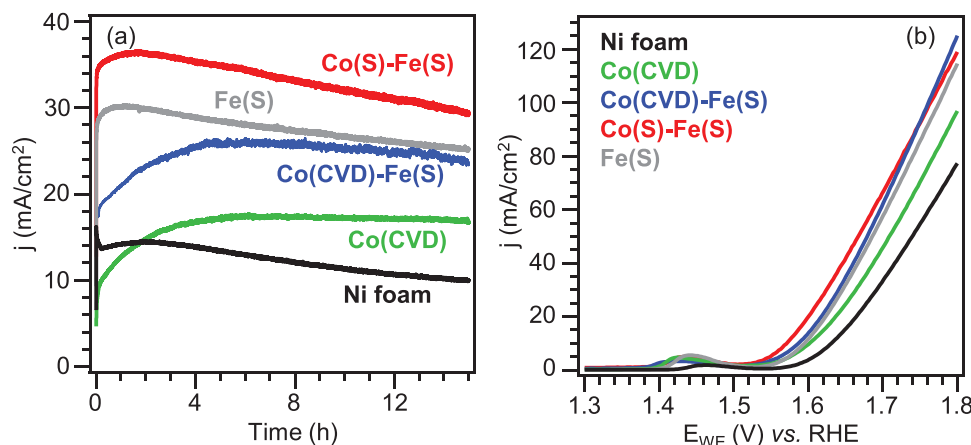

Figure 8. a) CA curves for the target specimens at a fixed potential of 1.65 V versus RHE. b) LSV curves collected on the target samples after CA experiments.

angle annular dark field-scanning transmission electron microscopy (HAADF-STEM), and EDXS measurements were carried out on a double aberration corrected JEM ARM200F (200 kV) cold FEG microscope, equipped with a large solid angle CENTURIO EDX detector, Orius CCD camera and Quantum GIF.

Electrochemical Studies: The electrocatalytic activity of the developed systems was tested using a standard three-electrode configuration, using an Autolab PGSTAT204 potentiostat/galvanostat. The coated Ni foams were used as working electrodes (WEs) in 1.0 M KOH solutions (pH = 13.85), whereas standard calomel (E_{SCE} = +0.246 V versus RHE; KCl 3 M) and a Pt wire were used as the reference (RE) and counter electrode (CE), respectively, as reported in the literature.[68] The SCE potential was periodically recalibrated after measurements to ensure a full reproducibility of the results obtained in repeated experiments, and no variations of its potential with respect to RHE were ever detected. For the bare Ni foam as well as for the fabricated electrocatalyst materials, the substrate was contacted with a metallic clamp, using a Teflon tape to limit the exposed area to 1.0 cm². No epoxy resin was used for electrode fabrication, since tests performed before measurements enabled to assess that the Ni foam pores (see also the top FE-SEM micrograph displayed in Figure 3) were big enough to prevent any capillary effect that might increase the exposed area and lead to an activity overestimation (see movie in the Supporting Information). This is in line with the fact that the electrodes were immersed in the solution following a previously described "dry" scenario.[69]

The measured potential values versus SCE (E_{SCE}) were converted into the RHE scale using the relation: $E_{RHE}(V) = E_{WE}(V) + E_{SCE}(V) + 0.059 \times pH$. The overpotential values were calculated at 10 mA cm⁻² as $E_{RHE}(V) - 1.23$, where 1.23 (in V) is the $E°$ value for O_2 evolution versus RHE. LSV curves were collected with a scan rate of 5 mV s⁻¹, while CV cycles were acquired between 0.8 and 1.6 V versus RHE at 50 mV s⁻¹. iR-correction was calculated assuming the cell resistance value as derived from EIS data (typically ≈1 Ω). EIS measurements were performed in the frequency range 10⁶–0.01 Hz, with 10 points per decade and 10 mV of modulation around a fixed potential of 1.55 V versus RHE.

Supporting Information

Supporting Information is available from the Wiley Online Library or from the author.

Conflict of Interest

The authors declare no conflict of interest.

Data Availability Statement

Research data are not shared.

[1] Y. Li, F.-M. Li, X.-Y. Meng, S.-N. Li, J.-H. Zeng, Y. Chen, *ACS Catal.* **2018**, *8*, 1913.

[2] M. Tahir, L. Pan, F. Idrees, X. Zhang, L. Wang, J.-J. Zou, Z. L. Wang, *Nano Energy* **2017**, *37*, 136.

[3] T. Reier, H. N. Nong, D. Teschner, R. Schlögl, P. Strasser, *Adv. Energy Mater.* **2017**, *7*, 1601275.

[4] N.-T. Suen, S.-F. Hung, Q. Quan, N. Zhang, Y.-J. Xu, H. M. Chen, *Chem. Soc. Rev.* **2017**, *46*, 337.

[5] G. Cheng, T. Kou, J. Zhang, C. Si, H. Gao, Z. Zhang, *Nano Energy* **2017**, *38*, 155.

[6] K. Zhu, F. Shi, X. Zhu, W. Yang, *Nano Energy* **2020**, *73*, 104761.

[7] Y. Wang, P. Che, X. Du, X. Zhang, *Int. J. Hydrogen Energy* **2020**, *45*, 28598.

[8] X.-Z. Liu, T. Tang, W.-J. Jiang, Q.-H. Zhang, L. Gu, J.-S. Hu, *Chem. Commun.* **2020**, *56*, 5374.

[9] W. Li, X. Gao, D. Xiong, F. Wei, W.-G. Song, J. Xu, L. Liu, *Adv. Energy Mater.* **2017**, *7*, 1602579.

[10] W. Li, X. Gao, X. Wang, D. Xiong, P.-P. Huang, W.-G. Song, X. Bao, L. Liu, *J. Power Sources* **2016**, *330*, 156.

[11] Y. Wang, T. Zhou, K. Jiang, P. Da, Z. Peng, J. Tang, B. Kong, W.-B. Cai, Z. Yang, G. Zheng, *Adv. Energy Mater.* **2014**, *4*, 1400696.

[12] Z. Chen, C. X. Kronawitter, B. E. Koel, *Phys. Chem. Chem. Phys.* **2015**, *17*, 29387.

[13] W. Zhu, R. Zhang, F. Qu, A. M. Asiri, X. Sun, *ChemCatChem* **2017**, *9*, 1721.

[14] F. Song, W. Li, J. Yang, G. Han, T. Yan, X. Liu, Y. Rao, P. Liao, Z. Cao, Y. Sun, *ACS Energy Lett.* **2019**, *4*, 1594.

[15] T.-J. Wang, X. Liu, Y. Li, F. Li, Z. Deng, Y. Chen, *Nano Res.* **2020**, *13*, 79.

[16] L. Xu, Q. Jiang, Z. Xiao, X. Li, J. Huo, S. Wang, L. Dai, *Angew. Chem., Int. Ed.* **2016**, *55*, 5277.

[17] Y. Tong, H. Mao, Y. Xu, J. Liu, *Inorg. Chem. Front.* **2019**, *6*, 2055.

[18] Y. Cheng, S. P. Jiang, *Prog. Nat. Sci: Mater. Int.* **2015**, *25*, 545.

[19] P.-P. Liu, Y.-Q. Zheng, H.-L. Zhu, T.-T. Li, *ACS Appl. Nano Mater.* **2019**, *2*, 744.

[20] L. Bigiani, A. Gasparotto, C. Maccato, C. Sada, J. Verbeeck, T. Andreu, J. R. Morante, D. Barreca, *ChemCatChem* **2020**, *12*, 5984.

[21] Y. Lu, C. Li, Y. Zhang, X. Cao, G. Xie, M. Wang, D. Peng, K. Huang, B. Zhang, T. Wang, W. Junsheng, Y. Huang, *Nano Energy* **2021**, *83*, 105800.

[22] S. Zhu, L.-a. Huang, Z. He, K. Wang, J. Guo, S.-e. Pei, H. Shao, J. Wang, *J. Electroanal. Chem.* **2018**, *827*, 42.

[23] H. Peng, W. Zhang, Y. Song, F. Yin, C. Zhang, L. Zhang, *Catal. Today* **2020**, *355*, 286.

[24] M. Q. Yu, Y. H. Li, S. Yang, P. F. Liu, L. F. Pan, L. Zhang, H. G. Yang, *J. Mater. Chem. A* **2015**, *3*, 14101.

[25] D. Zhang, J. Zhang, H. Wang, C. Cui, W. Jiao, J. Gao, Y. Liu, *J. Alloys Compd.* **2019**, *806*, 1419.

[26] L. Zhang, H. Li, B. Yang, Y. Zhou, Z. Zhang, Y. Wang, *J. Solid State Electrochem.* **2019**, *23*, 3287.

[27] N. K. Chaudhari, H. Jin, B. Kim, K. Lee, *Nanoscale* **2017**, *9*, 12231.

[28] F. Urbain, R. Du, P. Tang, V. Smirnov, T. Andreu, F. Finger, N. J. Divins, J. Llorca, J. Arbiol, A. Cabot, J. R. Morante, *Appl. Catal. B* **2019**, *259*, 118055.

2100763 (9 of 10)

**ADVANCED
SCIENCE NEWS**

www.advancedsciencenews.com

**ADVANCED
MATERIALS
INTERFACES**

www.advmatinterfaces.de

[29] W. Li, D. Xiong, X. Gao, W.-G. Song, F. Xia, L. Liu, *Catal. Today* **2017**, *287*, 122.

[30] Q. Xu, Q. Xu, Y. Su, H. Wu, H. Cheng, Y. Hui, N. Li, Z. Liu, *Curr. Nanosci.* **2014**, *11*, 107.

[31] J. R. Galán-Mascarós, *ChemElectroChem* **2015**, *2*, 37.

[32] F. Song, L. Bai, A. Moysiadou, S. Lee, C. Hu, L. Liardet, X. Hu, *J. Am. Chem. Soc.* **2018**, *140*, 7748.

[33] N.-I. Kim, Y. J. Sa, S.-H. Cho, I. So, K. Kwon, S. H. Joo, J.-Y. Park, *J. Electrochem. Soc.* **2016**, *163*, F3020.

[34] X. Du, C. Huang, X. Zhang, *J. Alloys Compd.* **2019**, *809*, 151821.

[35] K. Wu, D. Shen, Q. Meng, J. Wang, *Electrochim. Acta* **2018**, *288*, 82.

[36] X. Li, X. Du, X. Ma, Z. Wang, X. Hao, A. Abudula, A. Yoshida, G. Guan, *Electrochim. Acta* **2017**, *250*, 77.

[37] Y. Yang, C. Zhu, Y. Zhang, Y. Xie, L. Lv, W. Chen, Y. He, Z. Hu, *J. Phys. Chem. Solids* **2021**, *148*, 109680.

[38] A. QayoomMugheri, A. Tahira, U. Aftab, M. IshaqAbro, S. R. Chaudhry, L. Amaral, Z. H. Ibupoto, *Electrochim. Acta* **2019**, *306*, 9.

[39] H. Wu, S. Li, X. Lu, C. Y. Toe, H. Y. Chung, Y. Tang, X. Lu, R. Amal, L. Li, Y. H. Ng, *ChemPlusChem* **2018**, *83*, 934.

[40] J. Zhang, Q. Zhang, X. Feng, *Adv. Mater.* **2019**, *31*, 1808167.

[41] Y.-M. Zhao, F.-F. Wang, P.-J. Wei, G.-Q. Yu, S.-C. Cui, J.-G. Liu, *ChemistrySelect* **2018**, *3*, 207.

[42] D. Xiong, W. Li, X. Wang, L. Liu, *Nanotechnology* **2016**, *27*, 375401.

[43] G. Carraro, A. Gasparotto, C. Maccato, E. Bontempi, D. Barreca, *Surf. Coat. Technol.* **2016**, *307*, 352.

[44] A. Gasparotto, D. Barreca, D. Bekermann, A. Devi, R. A. Fischer, C. Maccato, E. Tondello, *J. Nanosci. Nanotechnol.* **2011**, *11*, 8206.

[45] D. Barreca, G. Carraro, A. Gasparotto, C. Maccato, M. E. A. Warwick, E. Toniato, V. Gombac, C. Sada, S. Turner, G. Van Tendeloo, P. Fornasiero, *Adv. Mater. Interfaces* **2016**, *3*, 1600348.

[46] G. Carraro, A. Gasparotto, C. Maccato, E. Bontempi, F. Bilo, D. Peeters, C. Sada, D. Barreca, *CrystEngComm* **2014**, *16*, 8710.

[47] G. Carraro, C. Maccato, A. Gasparotto, K. Kaunisto, C. Sada, D. Barreca, *Plasma Processes Polym.* **2016**, *13*, 191.

[48] G. Dong, H. Hu, X. Huang, Y. Zhang, Y. Bi, *J. Mater. Chem. A* **2018**, *6*, 21003.

[49] L. Bigiani, T. Andreu, C. Maccato, E. Fois, A. Gasparotto, C. Sada, G. Tabacchi, D. Krishnan, J. Verbeeck, J. R. Morante, D. Barreca, *J. Mater. Chem. A* **2020**, *8*, 16902.

[50] J. Y. Kim, H. Jun, S. J. Hong, H. G. Kim, J. S. Lee, *Int. J. Hydrogen Energy* **2011**, *36*, 9462.

[51] Pattern No. 042-1467, JCPDS **2000**.

[52] G. Zhang, J.-h. Li, *Chin. J. Chem. Phys.* **2018**, *31*, 517.

[53] L. Bigiani, D. Barreca, A. Gasparotto, T. Andreu, J. Verbeeck, C. Sada, E. Modin, O. I. Lebedev, J. R. Morante, C. Maccato, *Appl. Catal. B* **2021**, *284*, 119684.

[54] L. Bigiani, C. Maccato, T. Andreu, A. Gasparotto, C. Sada, E. Modin, O. I. Lebedev, J. R. Morante, D. Barreca, *ACS Appl. Nano Mater.* **2020**, *3*, 9889.

[55] J. F. Moulder, W. F. Stickle, P. E. Sobol, K. D. Bomben, *Handbook of X-ray Photoelectron Spectroscopy*, Perkin Elmer Corporation, Eden Prairie, MN, USA **1992**.

[56] D. Barreca, A. Gasparotto, O. I. Lebedev, C. Maccato, A. Pozza, E. Tondello, S. Turner, G. Van Tendeloo, *CrystEngComm* **2010**, *12*, 2185.

[57] J. Du, C. Li, Q. Tang, *Electrochim. Acta* **2020**, *331*, 135456.

[58] L. Zhuang, Y. Jia, T. He, A. Du, X. Yan, L. Ge, Z. Zhu, X. Yao, *Nano Res.* **2018**, *11*, 3509.

[59] S. Anantharaj, S. Kundu, S. Noda, *Nano Energy* **2021**, *80*, 105514.

[60] M. S. Burke, M. G. Kast, L. Trotochaud, A. M. Smith, S. W. Boettcher, *J. Am. Chem. Soc.* **2015**, *137*, 3638.

[61] T. Kosmala, D. Mosconi, G. Giallongo, G. A. Rizzi, G. Granozzi, *ACS Sustainable Chem. Eng.* **2018**, *6*, 7818.

[62] T. Kou, S. Wang, J. L. Hauser, M. Chen, S. R. J. Oliver, Y. Ye, J. Guo, Y. Li, *ACS Energy Lett.* **2019**, *4*, 622.

[63] T. Shinagawa, A. T. Garcia-Esparza, K. Takanabe, *Sci. Rep.* **2015**, *5*, 13801.

[64] L. Bigiani, A. Gasparotto, T. Andreu, J. Verbeeck, C. Sada, E. Modin, O. I. Lebedev, J. R. Morante, D. Barreca, C. Maccato, *Adv. Sustainable Syst.* **2020**, 2000177.

[65] Z. Li, M. Shao, H. An, Z. Wang, S. Xu, M. Wei, D. G. Evans, X. Duan, *Chem. Sci.* **2015**, *6*, 6624.

[66] W. B. McCormack, C. A. Sandy, UK Patent GB 2022088A, **1979**.

[67] https://imagej.nih.gov/ij/

[68] W. Luo, C. Jiang, Y. Li, S. A. Shevlin, X. Han, K. Qiu, Y. Cheng, Z. Guo, W. Huang, J. Tang, *J. Mater. Chem. A* **2017**, *5*, 2021.

[69] W. Zheng, M. Liu, L. Y. S. Lee, *ACS Energy Lett.* **2020**, *5*, 3260.